EFFECTS OF THE SURFACE ROUGHNESS AND THE POROSITY ON THE HIGH CYCLE FATIGUE BEHAVIOUR OF TI-6AL-4V ALLOY OBTAINED BY ADDITIVE MANUFACTURING PROCESS

Viet-Duc LE[1], Etienne PESSARD[1], Franck MOREL[1], Serge PRIGENT[2]

This work focuses on the influence of defects, including porosity and surface roughness, on the high cycle fatigue behaviour of the Ti-6Al-4V titanium alloy fabricated by the Laser Power Bed Fusion (LPBF) Additive Manufacturing (AM) process. In particular, the scatter and the statistical size effect are investigated. A vast fatigue test campaign has been undertaken, including two surface conditions (as-built and machined surfaces), and two specimen geometries. It was shown that a variety of crack initiation mechanisms, related to not only the pore type (gas and LoF pore) but also to the defect spatial position (surface or in-bulk) is the principal origin of the fatigue scatter for machined specimens. For the statistical scale or size effect, i.e., the change in the fatigue strength as a function of the loaded volume, it was shown that the changes in damage mechanisms are the first order factor that governs the size effect observed for the machined specimens. For the as-built specimens, these effects are less significant. In the last section, two fatigue strength modelling approaches that take into account both defect types are proposed.

INTRODUCTION

One of the most challenging problems in metal Additive Manufacturing (AM) is related to the presence of defects in the materials, which can be the origin of fatigue failures in structural components subjected to cyclic loads. The two main defect types found in AM materials are surface roughness and porosity. It has been shown in the literature that the presence of these defects significantly reduces the fatigue strength of the materials (Chan et al. [1], Greitermeier et al. [2], Günther et al. [3],Wycisk et al. [4]). In the work of Günther et al. [3] and Chastand et al. [5], the authors showed the presence of different pore types from which fatigue crack initiates such as Lack-of-Fusion (LoF) pores or gas pores. It is also shown that the fatigue behaviour corresponding to these pore types are very different. Regarding the effect of the as-built surface rougness on the fatigue behaviour, a detrimental impact has been observed on the fatigue behaviour with a decrease in the fatigue strength of up to 60% in comparison with machined specimens (Vayssette et al. [6], Nasab et al. [7], Masuo et al. [8]). The principal objective of this paper is to contribute to the comprehension of the effects of surface roughness and porosity, found in Laser Powder Bed Fusion (LPBF) additively manufactured Ti-6Al-4V titanium alloy on the fatigue behaviour in the high cycle fatigue regime. In particular, the fatigue scatter and the statistical scale effect are investigated by highlighting the roles of defect type, defect size and defect spatial location. In the second part of the article, two

[1] Arts et Metiers Institute of Technology, LAMPA, HESAM Université, Angers, FRANCE

[2] IRT Jules Verne, Bouguenais, FRANCE

fatigue modelling approaches are developed to predict the effects of the two defect types, the surface roughness and the porosity, on the fatigue strength.

Specimen fabrication

The titanium alloy used in this work is grade 23, Ti-6Al-4V ELI, with a standardized chemical composition by weight of Al 6%, V 4%, C ≤ 0.08%, Fe ≤ 0.25%, H ≤ 0.012%, N ≤ 0.05% and O ≤ 0.13%. The powders have a particle size range from 20 µm to 63 µm with a median size of 43 µm. The fatigue specimens were manufactured using a SLM 280HL machine with a standard parameter set, recommended by the machine manufacturer. In total, 68 fatigue specimens, distributed in four configurations, were fabricated (TABLE 1). The two specimen geometries used (Standard size and Small size) are shown in Figure 1. They have very different highly loaded volumes in order to investigate the statistical scale effect. For information, the $V_{80\%}$ (highly loaded volume in which the lowest stress is equal to the 80% of the highest stress in the whole specimen) under uniaxial tensile loads corresponding to these two geometries are respectively 2044 mm^3 and 206 mm^3.

TABLE 1: Four fatigue specimen configurations

Configuration (specimen size / surface state)	Number of specimens
Standard size / Machined	20
Small size / Machined	19
Standard size / As-built	14
Small size / As-built	15

All of the specimens were fabricated vertically (i.e. with a building direction of 90°). A post heat treatment (annealing at 850 °C for 2 hours followed by slow cooling) was used to relieve residual stresses. For the machined specimens, the as-fabricated gauge diameters were 10 mm for the standard size specimens and 7 mm for small size specimens. After machining 1 mm from the radius, the gauge diameters of the machined specimens were the same as the as-built specimens.

Microstructure, porosity and surface roughness

The microstructure, observed by using an optical microscope on chemically etched samples, was columnar with the grains orientation parallel to the building direction. This is in good agreement with work from literature (Thijs et al. [9], Le et al. [10]). For the as-built specimens, the microstructure in bulk was similar to that of the machined specimens. However, a sub-surface ring of 400 µm to 500 µm in thickness with a higher micro-hardness than the material in bulk (440 Hv0.2 versus 370 Hv0.2) was observed, probably due to the contouring strategy used in the specimen fabrication.

In terms of porosity, two types of pore were observed: gas pores and LoF pores, as shown in Figure *2*a and Figure *2*b. While gas pores were generally spherical with a size between 10 µm and 50 µm (in terms of $\sqrt{area}$), LoF pores, related mainly to the balling effect (Kasperovich and Hausmann [11], Le et al. [10]), have a very spread-out geometry and can be up to 350 µm in size.

The surface roughness was characterised using an optical 3D profilometer. A scan of an as-built surface is illustrated in Figure *2*c in which un-melted particles (in red) and local surface valleys (in

dark blue) can be seen. The global surface roughness, evaluated in zones with a size of 20 mm x 1 mm for standard size specimens and 6 mm x 1mm for small size specimens, is approximatively S_a=10µm for all of the as-built configurations.

FATIGUE BEHAVIOUR AND DAMAGE MECHANISMS

All fatigue tests were carried out at ambient temperature and pressure in laboratory air. The fatigue tests were conducted with a constant stress amplitude, a load ratio of R=0.1 and a frequency of 20 Hz. Tests were stopped after $2x10^6$ cycles. The run-out specimens that survived $2x10^6$ cycles were re-tested at a higher load. The principal aims of the re-tests is to gain access to the critical defect for all of the specimens in order to obtain a large enough database with a limited number of specimens. Because only the specimens that survived $2x10^6$ cycles were re-tested, the authors supposed that strengthening or cumulative damage effects are not significant at such a high number of cycles.

The Wöhler curves of the four configurations are shown in Figure 3. The fitting curves corresponding to a probability failure (Pf) of 10%, 50% and 90% were calculated using the Stromeyer equation [12], given as follows.

$$Log_{10}(N_f) = C - m.Log_{10}(S_{max} - S_0) \quad (1)$$

where N_f is the number of cycles to failure, S_{max} is the maximum stress, S_0 is the fatigue limit. C and m are material parameters.

It can be seen that for the machined specimens, the scatter of the fatigue strength at $2x10^6$ cycles is relatively high with a covariance, defined as the ratio between the standard deviation (Std) and the mean value (S_D) of the fatigue strength, of between 12% and 16%. Furthermore, it appears that the data are grouped into two different populations that are especially clear for the small size machined specimens. The first population, on the left of the diagram, includes points with N_f lower than 10^5 cycles, even for low applied stresses. The second population on the right includes specimens that have much higher fatigue lives with N_f between 10^5 and $2x10^6$ cycles. For the as-built specimens, the scatter in the S-N data is much lower, with a covariance between 5.5% and 8.6%. By comparing the fatigue strengths at $2x10^6$ cycles, it can be seen that the fatigue strength of the as-built specimens is approximately 40% to 60% lower than that of the machined specimens.

Regarding the scale effect, by comparing the fatigue strength at $2x10^6$ cycles, it can be stated that the fatigue strength of the small size specimens is higher than the standard size specimens (700 MPa vs 500 MPa). For as-built specimens, the scale effect is less significant.

Observations of the fatigue failure surfaces of all of the tested specimens using a scanning electron microscope reveal a large variety of crack initiation mechanisms. For the machined specimens, four mechanisms were identified: 1) LoF pores at the free surface (Figure *4*a); 2) LoF pores in the bulk (Figure *4*b); 3) Gas pores at the free surface (Figure *4*c); 4) Gas pores in the bulk (Figure *4*d). For the as-built specimens, two crack initiation mechanisms were observed: 1) LoF pores at the free surface (Figure *4*e) and 2) surface roughness without the presence of a pore (Figure *4*f).

ANALYSIS OF THE EFFECTS OF DEFECTS ON THE FATIGUE BEHAVIOUR

In order to analyse the effect of the defects on the scatter and the scale effect, a summary of the number of occurrences of each crack initiation mechanisms, observed in all batches, is given in

TABLE 2. Furthermore, S-N diagrams in which the different crack initiation mechanisms are highlighted are shown in Figure 5a for the machined specimens and in Figure 5b for the as-built specimens.

It can be observed, for the machined specimens, that the fatigue behaviour corresponding to the four crack initiation mechanisms are very different. The LoF pores (with an average mean size of 150 µm in $\sqrt{area}$) located at the free surface are the most detrimental defect type while the gas pores (with an average mean size of 30 µm in $\sqrt{area}$) in bulk seem to be the least harmful defect type. Another interesting observation is the effect of the defect spatial position. For the same LoF pore type, the pores located on the specimen surface are more detrimental than the ones in bulk, given that the pore size distributions are similar. From these observations, it can be concluded that the high scatter observed for the machined specimens is caused principally by the large variety of crack initiation mechanisms. For the as-built specimens, the S-N diagram shown in Figure 5b demonstrates that there is no significant difference in terms of the fatigue strength between the two crack initiation mechanisms. This observation is quite surprising because when linked to the defect size as illustrated in Figure *4*e, the impact of a LoF pore with a depth of approximately 400 µm is equivalent to a surface roughness defect with a depth of 20 µm (Figure *4*f).

Regarding the scale effect observed for the machined specimens, it can be seen in TABLE *2* that the probability of occurrence of LoF pores at the crack initiation sites is higher for the standard size specimens than the for the small size specimens, knowing that the LoF pore size distributions are similar. Because the fatigue strength related to the LoF pore mechanisms is significantly lower than for the other pore type (i.e. gas pores), it can be concluded that the scale effect observed for the machined specimens is linked principally to the change of the crack initiation mechanism and not to the change of the critical pore size. For the as-built specimens, the change of crack initiation mechanism can also be stated to occur. However, because of the similarity in the fatigue strengths of these two mechanisms, the scale effect is less pronounced for the as-built specimens.

TABLE 2: A summary of the sample numbers with different crack initiation mechanisms in each configuration

Configuration	LoF pore on surface Nb (Pct.)	LoF pore in bulk Nb (Pct.)	Gas pore on surface Nb (Pct.)	Gas pore in bulk Nb (Pct.)	Surface roughness Nb (Pct.)
Standard size - Machined	10 (50%)	8 (40%)	2 (10%)	0 (0%)	0 (0%)
Small size - Machined	7 (37%)	5 (26%)	4 (21%)	3 (16%)	0 (0%)
Standard size – As-built	11 (85%)	0 (0%)	0 (0%)	0 (0%)	2 (15%)
Small size – As-built	7 (47%)	0 (0%)	0 (0%)	0 (0%)	8 (53%)

MODELLING OF THE FATIGUE STRENGTH TAKING INTO ACCOUNT THE DEFECTS

In this section, two fatigue modelling approaches are developed to deal with the two observed defect types, porosity and surface roughness. The first one takes into account the effect of porosity on the fatigue strength for machined specimens (i.e. without as-built surface roughness). More precisely, by using a probabilistic approach, the change in the crack initiation mechanism when changing the loaded volume can be modelled, in combination with a model taking into account the pore size effect. The second approach models the effect of the as-built surface roughness on the

fatigue strength. Even though this mechanism is not the main mechanism observed for the as-built specimens in this study, modelling of the surface roughness effect is always of interest in fatigue design. Finally, the mechanism of LoF on surface in as-built specimens, that is the main mechanism observed for the as-built specimens, should be modelled as a combination of *i)* porosity effect model and *ii)* roughness effect model, as proposed in the work of Pomberger et al. [13]. This approach will be developed in the future and is not presented in this paper.

1st Approach: modelling the effect of porosity

The concept behind the first modelling approach is shown in Figure *6*. The principal aim of this approach is to model the scale effect observed for machined specimens, which is governed principally by changes in the crack initiation mechanism and not by the change of the critical pore size distribution. For this reason, it is assumed that the critical pore size distribution, measured at the crack initiation sites, does not change as a function of the loaded volume. A deterministic model linking the mean fatigue strength S_D to the pore size $\sqrt{area}$ is obtained by using a corrected fatigue strength (in terms of the maximum stress) S_{max} and the Stromeyer model, as given by Eq. (1) and (2). The model parameters are empirically obtained by fitting with the experimental S-N data. More details of this approach can be found in a previous publication (Le et al.[14]). The distribution of the fatigue strength for each crack initiation mechanism (LoF pore on surface (PDF_1), LoF pore in bulk (PDF_2), Gas pore on surface (PDF_3)) is then calculated by combining the deterministic model "$\sqrt{area}$-S_D" and the critical pore size distribution.

$$\text{Corrected } S_{max} = S_{max}\left(\frac{\sqrt{area}}{\sqrt{area}_0}\right)^{s'} \quad (2)$$

$$Log_{10}(N_f) = C - m.Log_{10}(\text{Corrected } S_{max} - S_0) \quad (3)$$

The probability of occurrence of the three crack initiation mechanisms, LoF pore on surface (P_1), LoF pore in bulk (P_2) and Gas pore on surface (P_3), are calculated from the volume density of LoF pore, λ, defined as the number of LoF pores per mm^3. Crack initiation from internal gas pores (with a probability of occurrence less than 10%) is neglected in the present approach. The volume density of LoF pore λ is determined thanks to an inverse methodology, inspired by the work of Chandran [14] and presented in detail in [15]. In short, by assuming that the spatial distribution of LoF pores is completely random, the probability of occurrence of each crack initiation mechanism is calculated for several λ values and for a given volume. The results are then compared with the probabilities of occurrence of the crack initiation mechanisms observed experimentally on the failure surfaces in order to find a reasonable λ value. As shown in Figure 7, the correlation between the simulation curves and experimental data points for the probability of occurrence of each crack initiation mechanism shows that the density of LoF pore can be estimated to be between 10^{-3} to 10^{-2} pores per mm^3. A value $\lambda = 10^{-2}$ pore/mm^3 is used in the next step. Finally, the global fatigue strength distribution corresponding to a given loaded volume is calculated as the sum of the fatigue strength distributions of all of the crack initiation mechanisms. Figure 8 shows the simulated fatigue strength distributions for the standard size and the small size specimens. The experimental fatigue strengths obtained by extrapolating the S-N data to a fatigue life of $2x10^6$ cycles using Eq. (2) are also shown in order to compare with the simulated distributions.

Firstly, it can be seen that a variety of crack initiation mechanisms are taken into account in this approach, which results in more than one peak in the fatigue strength distributions. The scale effect

is also predicted when comparing the fatigue strength distributions between the standard size and small size specimens. In fact, it can be seen that the highest peak in the fatigue strength distribution for standard size specimens corresponds to the LoF pore on surface mechanism while for small size specimens, the highest peak corresponds to the LoF pore in bulk mechanism. This change results in an increase in the fatigue strength at a failure probability of 50% (approximately 450 MPa for the standard size and 550 MPa for the small size specimens). Finally, it can be seen that the predicted fatigue strength distributions are in good agreement with the extrapolated fatigue strengths.

2nd Approach: modelling the effect of the surface roughness

In the literature, numerous fatigue approaches take into account surface roughness via local surface valley parameters. Two characteristics of local surface valleys that are often used to model the fatigue strength are the depth (characterized by maximum profile valley depth *Rv* or *Sv* in case of surface valley) and the valley radius ρ ([13]). In the current work, a surface profile processing methodology has been developed in order to be able to determine these two parameters. This methodology consists of, firstly, applying tilting corrections and a Gaussian regression filter on the surface profiles extracted from surface topography obtained by a Bruker's 3D optical profilometer. A convolution filter with a Hann window is then applied in order to convert the numerical profile to a smooth profile, which makes it possible to calculate the curvature, κ, and then the radius of curvature, ρ, at every point of the profile. The mathematical formulations of the curvature and the radius of curvature are given as follows in which x, y are the Cartesian coordinates of each point on the profile and x', x'', y', y'' are the first and second derivatives of the coordinates.

$$\kappa = \frac{x'y'' - y'x''}{\left(x'^2 + y'^2\right)^{3/2}} \qquad \rho = \frac{1}{\kappa} \tag{4}$$

Figure 9a shows an as-built surface profile with a cartography of the radius of curvature at each point of the profile. The same diagram for a machined surface is shown in Figure 9b for comparison. It can be seen that for the LBPF as-built surface profile, the local valleys can reach 35 µm in depth while the radius of curvature at the valley bottoms is very small, can reach ρ=1 µm. For the machined surface, the local surface valleys are much more regular with lower *Rv* values and larger radii at the valley bottoms. From the R_v and ρ values, the stress concentration factor, K_t, and the notch sensitivity factor, K_f, are calculated using the Peterson approach (Peterson [16]) and the approach proposed by Lukas and Klesnil [17] (Eq. (4)). A value of the material parameter a_0 of 0.01 mm is chosen so that the predicted fatigue strength distribution matches with the experimental result. The distribution of the K_f is then calculated by using the extreme value theory (Makkonen et al. [18]). Finally, the fatigue strength (S_D) distribution of the as-built specimens is calculated from the fatigue strength of defect-free material $S_{D,0}$. Thanks to fatigue tests conducted on HIP machined specimens for which the fatigue crack initiation is linked to the microstructure without the presence of defects, a value of $S_{D,0}$=720 MPa was found. A similar value is also reported in the literature ([2], [19]) for a load ratio of R=0.1 and a fatigue life of 2x10^6 cycles.

$$K_t = 1 + 2\sqrt{\frac{R_v}{\rho}} \qquad K_f = \frac{K_t}{\left(\frac{a_0 \times 4.5}{\rho} + 1\right)^{1/2}} \qquad S_D = \frac{S_{D,0}}{K_f} \tag{5}$$

Figure 10 shows the distributions of K_f and the fatigue strength at 2x10^6 cycles (S_D) for machined surface and as-built surface specimens. The fatigue strengths extrapolated from the S-N data of the only as-built specimens related to the surface roughness mechanism are also shown for comparison.

The predicted mean value of the K_f factor is approximately 2.25 for as-built surfaces, resulting in a fatigue strength of approximately 320 MPa, which is in good agreement with the experimental result. For machined specimens, a mean value of K_f = 1.1 is estimated, resulting in a fatigue strength approximately 10% lower than the $S_{D,0}$ value. This decrease seems be over-estimated for machined surface specimens with a S_a lower than 0.5 µm (Abroug et al. [20]). One possible explanation is that for very small local surface valleys such as in a machined surface, the Lukas approach cannot take into account the "small crack" phenomenon and hence, underestimates the fatigue strength. In summary, the proposed approach to model the surface roughness effect on the fatigue strength is potentially feasible for engineering fatigue design. However, further validation with different surface roughness levels are necessary to enhance the approach.

DISCUSSION AND CONCLUSIONS

This work deals with the scatter and the statistical scale effect in fatigue behaviour of a LBPF Ti-6Al-4V alloy. It is shown that the high scatter observed on the machined specimens is governed principally by the large variety of crack initiation mechanisms (LoF pores or gas pores; surface or internal pores). In fact, the fatigue strength changes significantly from one mechanism to another, for example the fatigue strength related to LoF pores on surface is more than 1.5 times lower than the value linked to gas pores. The scale effect is also pronounced for the machined specimens and can be explained by the change of the occurrence probability of each mechanism when changing the loaded volume. For the as-built specimens, these effects are much less pronounced even though there are multiple crack initiation mechanisms, which can be explained by the similarity in fatigue strengths of all of the mechanisms.

In order to model the effects of the two defect types, the porosity and the surface roughness, on the fatigue strength, two approaches have been developed. The first one models the effect of porosity by using a probabilistic approach that considers all of the crack initiation mechanisms. The model takes into account pore size and location as well as LoF pore density. Thanks to this approach, the change in crack initiation mechanism when changing the loaded volume can be simulated and hence the scale effect can be predicted. One of the key parameters of this model is the LoF pore density for which the estimation is not simple. In this work, an inverse methodology was used. This approach is not perfect because the result depends on the number of observations realised on fatigue failure surfaces, which is often not large enough to be statistically representative. Another way, would be to use tomography observations. However, it was observed in the present project that compressive residual stresses on the machined surfaces makes the surface crack initiation mechanism less likely to occur. Consequently, the use of the LoF pore density measured by tomography observations in this model results in a highly conservative predicted fatigue strength.

The second approach models the effect of surface roughness on fatigue strength. A surface profile processing algorithm has been developed to determine the depth and the radius of curvature at the bottom of local profile valleys. These two parameters are then used to calculate the notch sensitivity factor thanks to classical approaches and the associated fatigue strength. It should be noted that this model does not take into account the interaction between in-bulk pores and surface roughness and should be used when crack initiation is only related to the surface roughness. For the case where pores are present at the crack initiation sites, a mixed model that combines both developed approaches using a weight factor could be considered.

Both of these models have been validated initially with the data that was used to develop the models. Further validation with materials that have significant changes in terms of defects characteristics (such as LoF pores density for the first model; surface roughness level for the second model) needs to be done. However, both approaches that have been developed in light of the observed the crack initiation mechanisms and are potentially feasible for engineering fatigue design.

ACKNOWLEDGEMENT

This study is part of the FASICOM project, managed by the IRT Jules Verne (French Institute of Research and Technology in Advanced Manufacturing Technologies for Composite, Metallic and Hybrid Structures). The authors wish to associate the following industrial partners with this work: ADDUP, AIRBUS, ArianeGroup and General Electric.

REFERENCE LIST

[1] Chan, K. S., Koike, M., Mason, R. L., Okabe, T., *Metall. Mater. Trans. A,* vol. 44, pp. 1010-1022, 10 2012.

[2] Greitemeier, D., Palm, F., Syassen, F., Melz, T., *Int. J. Fatigue.,* vol. 94, pp. 211-217, 1 2017.

[3] Günther, J., Krewerth, D., Lippmann, T., Leuders, S., Tröster, T., Weidner, A., Biermann, H., Niendorf, T., *Int. J. Fatigue.,* vol. 94, pp. 236-245, 1 2017.

[4] Wycisk, E., Solbach, A., Siddique, S., Herzog, D., Walther, F., Emmelmann, C., *Phys. Procedia,* vol. 56, pp. 371-378, 2014.

[5] Chastand, V., Quaegebeur, P., Maia, W., Charkaluk, E., *Mater. Charact.,* vol. 143, pp. 76-81, 2018.

[6] Vayssette, B., Saintier, N., Brugger, C., May, M. E., Pessard, E., *Int. J. Fatigue.,* vol. 123, pp. 180-195, 2019.

[7] Nasab M. H., Romano S., Gastaldi D., Beretta S., Vedani M., *Addit. Manuf.,* p. 100918, 2019.

[8] Masuo, H., Tanaka, Y., Morokoshi, S., Yagura, H., Uchida, T., Yamamoto, Y., Murakami, Y., *Int. J. Fatigue,* vol. 117, p. 163–179, 12 2018.

[9] Thijs, L, Verhaeghe, F., Craeghs, T., Humbeeck, J. V., Kruth, J.-P., *Materialia,* vol. 58, p. 3303–3312, 5 2010.

[10] Le, V.-D., Pessard, E., Morel, F., Edy, F., *Eng. Fract. Mech.,* vol. 214, pp. 410-426, 2019.

[11] Kasperovich, G., Hausmann, J., *J. Mater. Process. Technol.,* vol. 220, p. 202–214, 6 2015.

[12] Stromeyer, C. E., *Proc. R. Soc. Lond. Series A, Containing Papers of a Mathematical and Physical Character,* vol. 90, p. 411–425, 7 1914.

[13] Pomberger, S., Stoschka, M., Aigner, R., Leitner, M., Ehart, R., *Int. J. Fatigue.,* vol. 133, p. 105423, 4 2020.

[14] Chandran, K. S. R., *Nat. Mater.*, vol. 4, p. 303–308, 3 2005.

[15] Le, V.-D., Pessard, E., Morel, F., Prigent, S., *Int. J. Fatigue.*, vol. 140, p. 105811, 11 2020.

[16] Peterson, R, *Metal Fatigue*, McGraw-Hill, NY. éd., G. Sines et J. L. Waisman, Éds., 1959.

[17] Lukáš, P., Klesnil, M., *Mat. Sci. Eng.*, vol. 34, p. 61–66, 6 1978.

[18] Makkonen, L., Rabb, R., Tikanmäki, M., *Mat. Sci. Eng.: A* , vol. 594, pp. 68-71, 2014.

[19] Hrabe, N., Gnäupel-Herold, T., Quinn, T., *Int. J. Fatigue.*, vol. 94, pp. 202-210, 2017.

[20] Abroug, F., Pessard, E., Germain, G., Morel, F., *Int. J. Fatigue.*, vol. 116, p. 473–489, 11 2018.

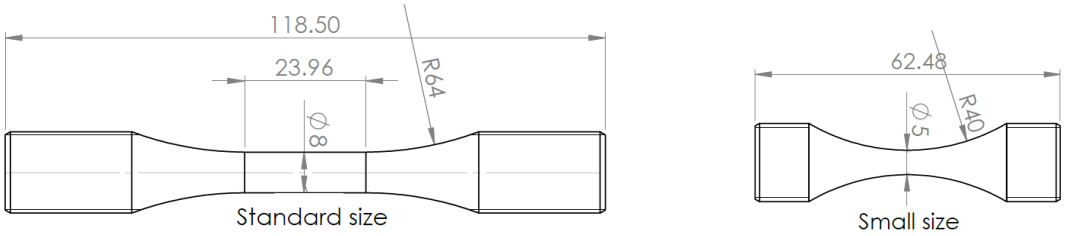

Figure 1: Two fatigue specimen geometries: Standard size and small size

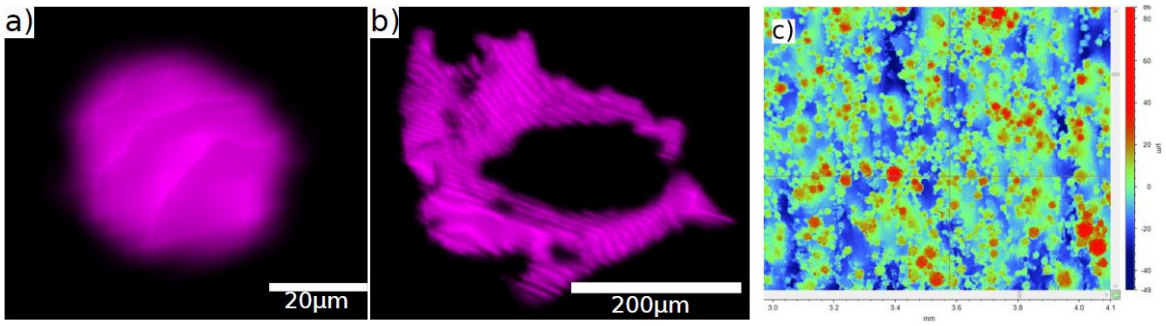

Figure 2: a) A gas pore, b) a LoF pore observed by X-ray micro-tomography and c) As-built surface topography scanned by a 3D profilometer

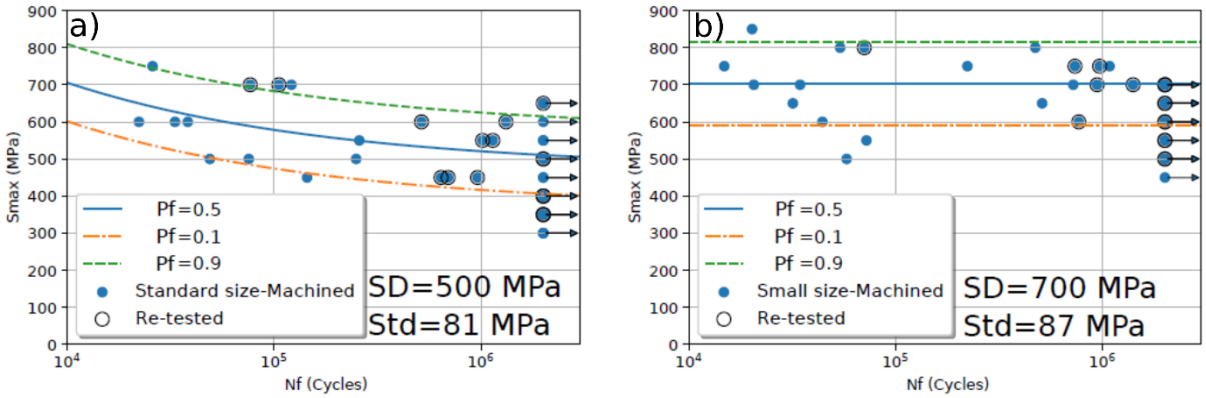

Figure 3: Wöhler curves for (a) standard size machined specimens and (b) small size machined specimens, (c) standard size as-built specimens, (d) small size as-built specimens

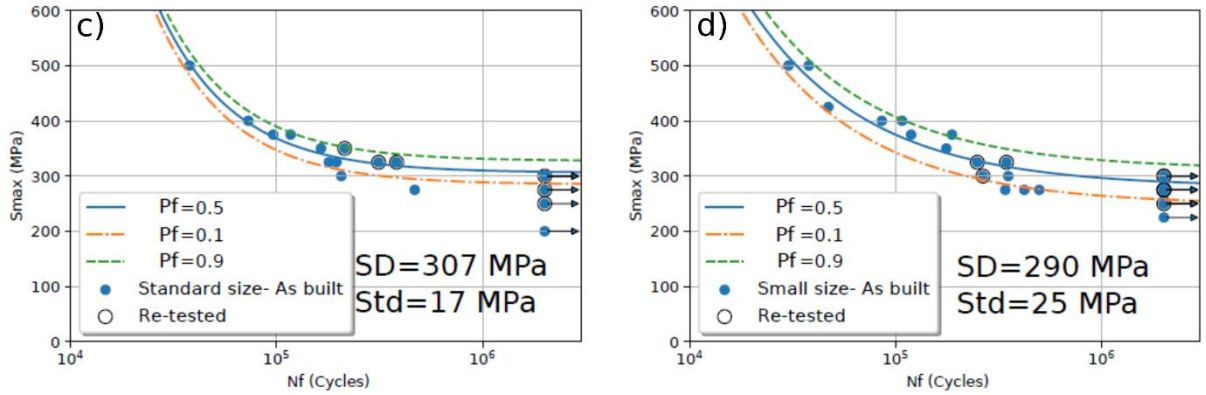

Figure 3 (continued)

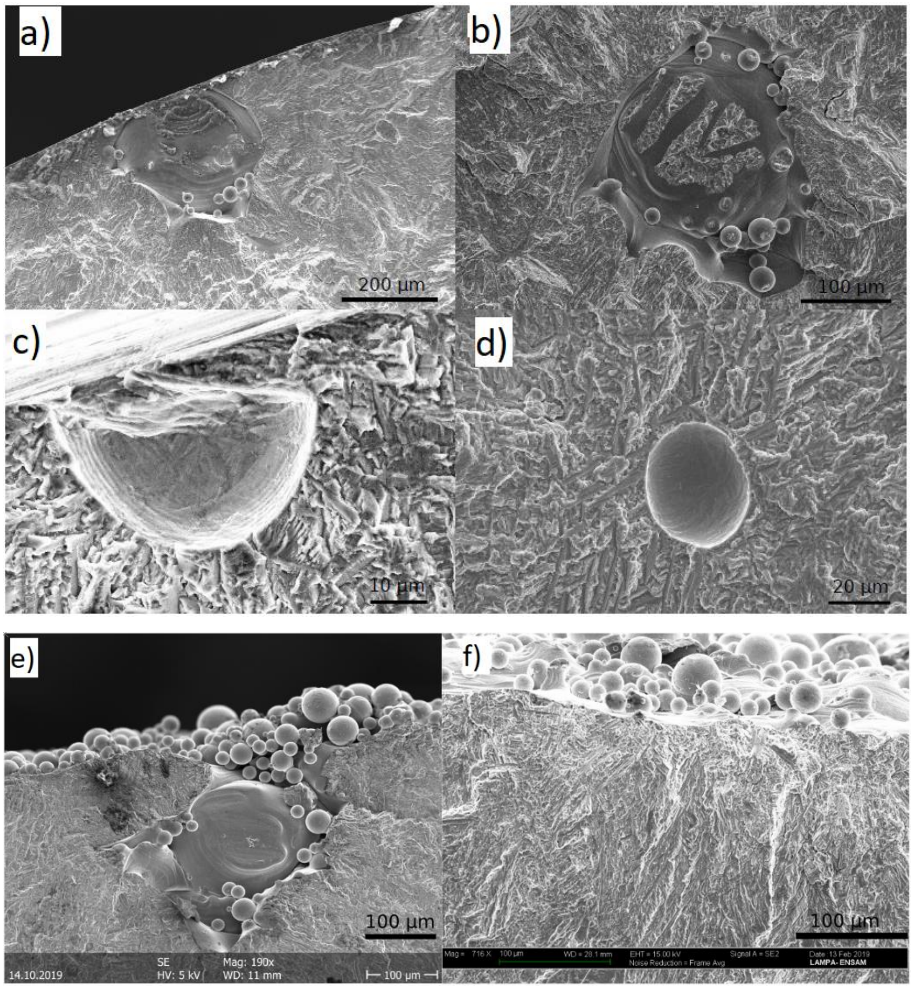

Figure 4: The defect types observed at the crack initiation sites: for the machined specimens, (a) LoF pore at the surface, (b) LoF pore in the bulk, (c) Gas pore at the surface, (d) Gas pore in the bulk; for as-built specimens e) crack initiation from a LoF pore and f) crack initiation from the surface roughness

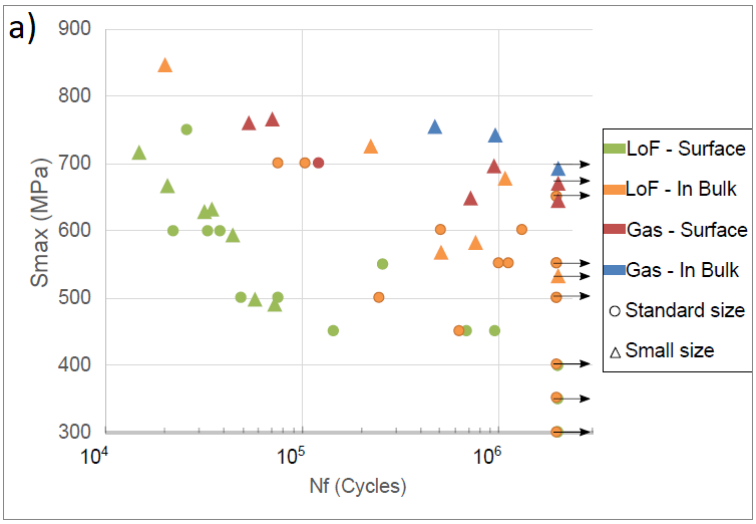

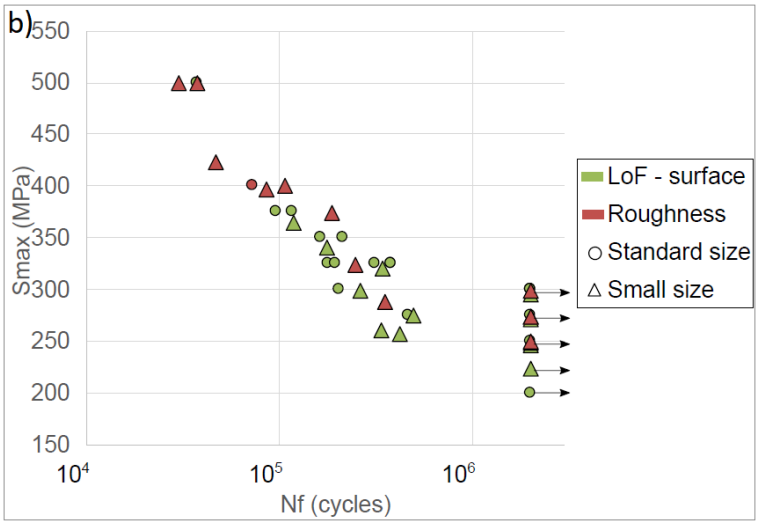

Figure 5: Correlation between the fatigue strength and the fatigue damage mechanisms for a) machined specimens and b) as-built specimens

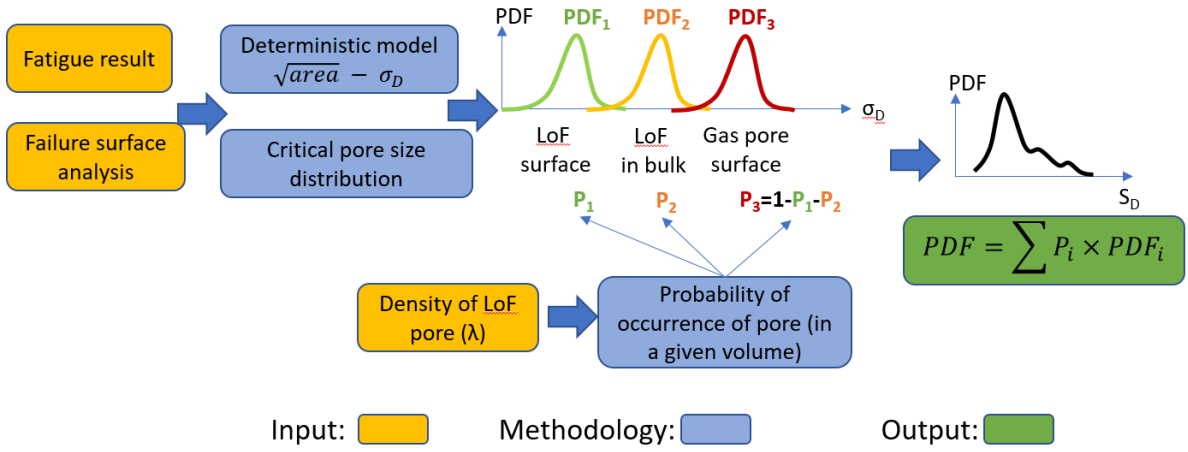

Figure 6: Description of the probabilistic approach to model the effect of porosity on fatigue strength

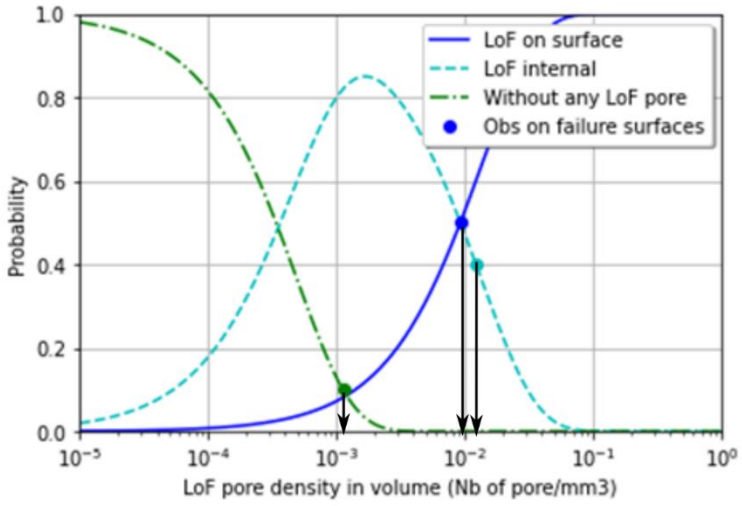

Figure 7: Identification of the LoF pore density value by the inverse methodology. Curves – probability of occurrence of each crack initiation mechanism simulated; Dots – Probability of occurrence measured of each mechanism measured on failure surface

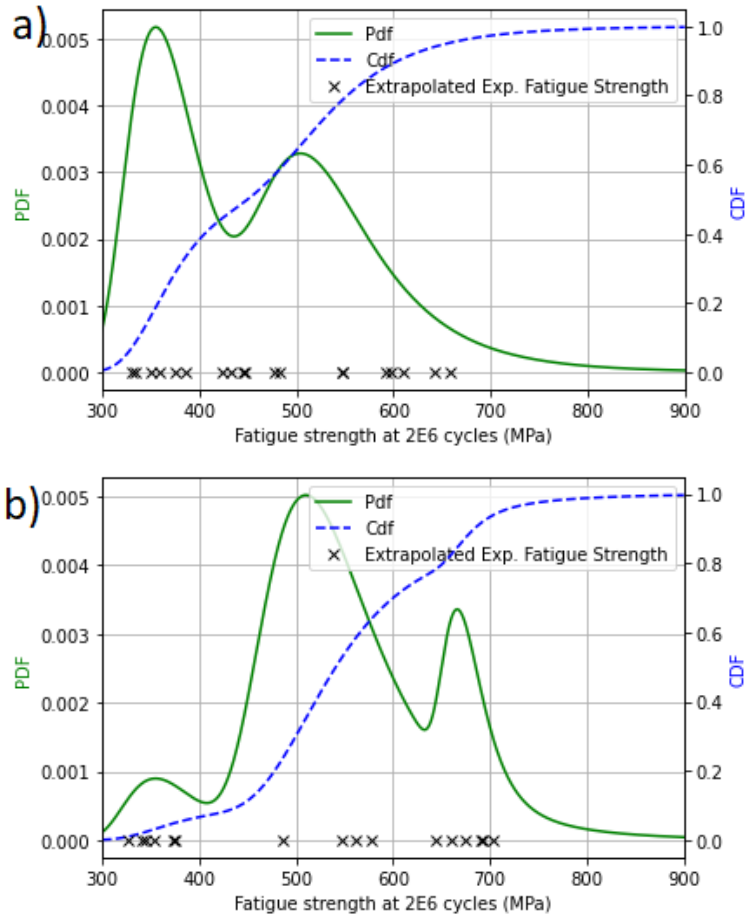

Figure 8: Predicted fatigue strength distribution for a) Standard size and b) Small size with a LoF pore density $\lambda=10^{-2}$ pore/mm^3

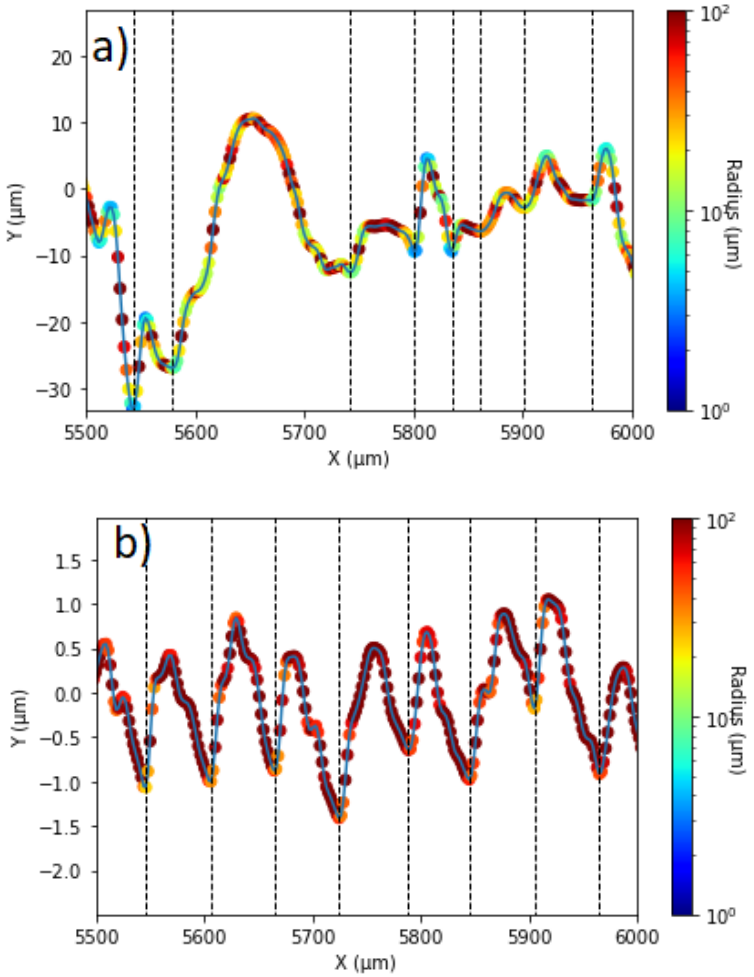

Figure 9: Surface profile (extracted from 3D surface topography scanned by the profilometer for a) LBPF as-built surface and b) machined surface

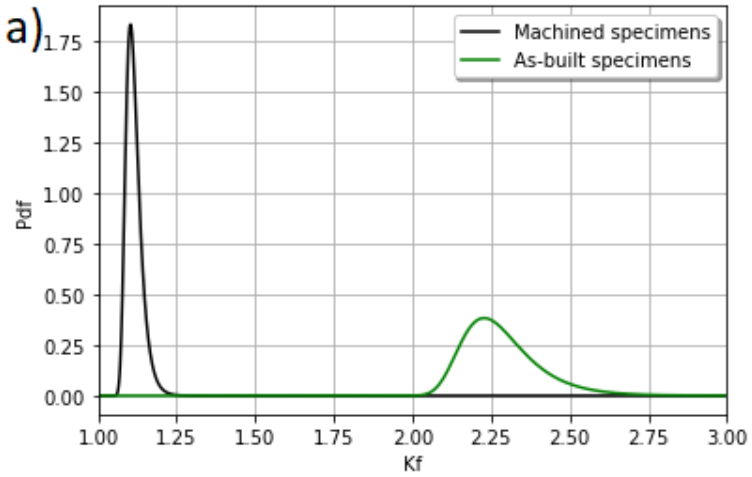

Figure 10: (a) Extreme value distributions of K_f and (b) simulated fatigue strength distribution

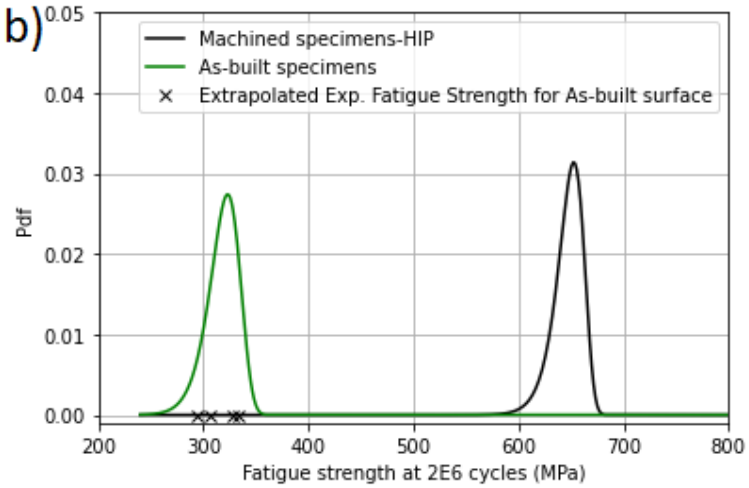

Figure 10 (continued)